Infrared Physics & Technology 53 (2010) 363–371

Contents lists available at ScienceDirect

Infrared Physics & Technology

journal homepage: www.elsevier.com/locate/infrared

Quantitative determination of subsurface defects in a reference specimen made of Plexiglas by means of lock-in and pulse phase infrared thermography

Roberto Montanini *

Department of Industrial Chemistry and Materials Engineering, University of Messina, Viale F. Stagno D'Alcontres 31, I-98166 Sant'Agata (ME), Messina, Italy

ARTICLE INFO

Article history:
Received 14 April 2010
Available online 16 July 2010

Keywords:
Infrared thermography
Lock-in thermography
Pulse phase thermography
Temperature measurements
Thermal diffusivity
Non-destructive testing and evaluation (NDT&E)

ABSTRACT

Lock-in and pulse phase infrared thermography measurement techniques have been exploited for quantitative assessment of subsurface defects in a reference specimen made of Plexiglas. Radiometric thermal images were post-processed using a contrast approach in the frequency domain, allowing defect depth to be resolved with a combined standard uncertainty of about 5% for thicknesses up to 3.6 mm. Conversely, significant radial heat diffusion next to the boundary of the discontinuities made accurate sizing of deeper subsurface defects more difficult, resulting in a combined standard uncertainty of about 17% for a 10 mm diameter flat-bottomed hole of 3.6 mm deep. The obtained results demonstrate the potentiality of active thermography as a fast, powerful contactless NDE measurement tool.

1. Introduction

Quantitative assessment and periodical monitoring of subsurface discontinuities in manufactured parts are fundamental steps towards the achievement of high quality/high reliable end products. Although well established non-destructive evaluation (NDE) methods are available today for the inspection of end products in service, nevertheless there is a strong interest in developing advanced measurement techniques which allow for fast, non-contact, and in situ inspection of large structures.

Among emerging technologies, as a result of remarkable progresses in the fabrication of high sensitive focal plane array detectors, infrared thermography (IRT) has gained much consideration in the scientific community [1,2]. During the last few years active thermography has been recognized as a powerful measurement tool for detecting surface and subsurface features in different kinds of materials, such as metals, composites, and polymers [3–8]. Most demonstrations however are limited to ascertain the presence of a discontinuity rather than measuring its features.

In contrast to the conventional passive approach, active thermography requires an excitation source to induce thermal contrast between defected and sound regions and a high thermal sensitivity IR camera to measure the resulting surface temperature response in the stationary or transient regime. Measurement information is given in a C-scan like mode in terms of gray levels or false colours digital images which need to be further post-processed in order to obtain quantitative data (i.e., defects depth and size estimation).

Basically two different measurement approaches can be used: modulated lock-in thermography (LT) and pulse thermography (PT).

Lock-in thermography [9–11] makes use of a modulated optical stimulation to heat the sample, thus producing a thermal wave which propagates through the thickness of the test sample. As the thermal wave encounters a discontinuity it undergoes reflections because of the locally changed heat propagation parameters. The reflected wave interferes with the surface wave giving rise to a stationary oscillating temperature field, which is remotely measured through its thermal infrared emission by the IR camera. Amplitude and phase images of the reconstructed thermal wave are computed for each heat-generating frequency using the Fourier transform algorithm. These two quantities are used to present the relevant information about subsurface discontinuities. Lock-in thermography has been proposed to detect areas of disbond in coatings [3], delaminations, impact damage and inclusions of spurious materials in composite materials [3,5,6], flat-bottomed hole defects in steel [12,13] and carbon fibre composite plates [14], delaminations of veneered wood [15], to visualize fibre orientation in composites [16], and to identify detachments or cracks in frescoes [17–19]. One main limitation of lock-in thermography is that, in order to obtain sufficient phase response over the range of depths at which a defect is expected to be found, the appropriate modulation frequency must be chosen. Besides, testing time can become quite long as very low frequencies have to be used to detect deeper defects.

* Tel.: +39 90 397 72 48; fax: +39 90 397 74 64.
E-mail address: rmontanini@ingegneria.unime.it

1350-4495/$ - see front matter © 2010 Elsevier B.V. All rights reserved.
doi:10.1016/j.infrared.2010.07.002

Another approach is pulse thermography, in which energy is delivered to the object surface by means of one or more sudden heat pulses and its surface temperature evolution is monitored by acquiring thermograms in time sequence during the transient heating (cooling) phase [4,7,12,17,18]. A subsurface discontinuity alters the thermal path of the heat flow developing a localized surface temperature contrast over the damaged area. Quantitative data about depth, size and nature of the discontinuity can be obtained by analyzing the relative time and the thermal contrast of the measured images sequence. The heat source can be positioned either on the opposite part of the test sample with respect to the IR camera (transmission mode) or on the same side (reflection mode). The detectability of defects (i.e., the achievement of a proper thermal contrast between defected and sound regions) depends on several factors, which include thermal diffusivity of the material, environmental conditions and instrument sensitivity. In addition, it has to be remarked that measurements performed by means of the pulsed thermographic method are affected by local variation of the emissivity coefficient and by non-uniform heating of the surface, that can mask the defect visibility. The emissivity problem may be overcome by painting the surface, but this could be a solution only for parts where this surface finish is tolerable. The uniformity of surface heating may be improved by using the lateral heating technique described by Grinzato et al. [19].

A measurement technique which combines the advantages of both LT and PT without sharing their drawbacks is pulse phase thermography (PPT), which has been first proposed by Maldague and Marinetti [20,21]. The specimen is pulse heated as in pulsed thermography and the mix of frequencies of the thermal waves launched into the specimen is unscrambled by computing the Fourier transform of the temperature evolution over the field of view; the phase, or magnitude, image can be presented as in modulated lock-in thermography. The fact that pulse phase thermography sorts available information coherently in term of frequencies brings interesting features with respect to the more traditional contrast approach used in pulse thermography.

In this paper lock-in and pulse phase infrared thermography measurement techniques have been exploited to gather quantitative information about subsurface defects. A reference specimen made of Plexiglas, with known flat-bottomed hole defects of different depth, was used for the experiments. By proper post-processing of phase thermal images measured using either modulated or pulsed optical excitation, depth and size of flat-bottomed hole defects were determined and the measurement uncertainty assessed. Merits and limitations of the proposed approach, based on a one-dimensional approximation of the heat flow, as well as metrological aspects related to possible interference inputs, are discussed thoroughly.

2. Materials and methods

All the experimental tests were performed using a 14-bit digital output IR camera (mod. Emerald MWIR, Cedip Infrared Systems, Croissy Beaubourg, France), equipped with a medium resolution (320 × 240 pixel) cooled InSb focal plane array and a 25 mm optical lens. The IR camera operates in the MWIR (3–5 μm) wavelength spectral range and has a thermal resolution of about 25 mK at 25 °C (NETD, Noise Equivalent Temperature Difference). The data acquisition system was controlled by a personal computer which allows the integration time to be varied in the range 10 μs to 5 ms. The actual frame rate was set to 80 frames/s.

Synchronization of external analogue signals were accomplished by the lock-in module integrated into the infrared camera.

Images acquisition, camera configuration and non-uniformity correction (NUC) calculations were carried out using DisplayIMG ver. 2.6 (Edevis GmbH, Stuttgart, Germany) and Cirrus ver. 5.80.2 (Cedip Infrared Systems, Croissy Beaubourg, France) software. Digital images were post-processed using Labview™ ver. 8.5 (National Instruments, Austin, Texas).

2.1. Reference specimen preparation

A reference PolyMethylMethAcrylate (PMMA) specimen, with known flat-bottomed hole defects of different depth, has been prepared as shown in Fig. 1. The specimen has a circular shape and presents sixteen 10 mm diameter holes, whose depth from the front side surface ranges from 0.6 mm (top right corner) to 3.6 mm (bottom left corner). Defect depth thus refers to the residual thickness of material between the ending base of the hole and the frontal sound surface of the specimen, which was painted with opaque black paint to uniform emissivity and reduce reflections.

2.2. Measuring principle

Preliminary tests have been carried out in order to evaluate the influence of different working parameters on the amplitude and phase response. The following factors were investigated: distance between the IR camera and the test sample, relative orientation of the IR camera axis with respect to the heating source, heating power and number of pre-heating cycles required to achieve stationary response (lock-in measurements), heat pulse duration and sampling rate (pulse phase measurements). An optimum combination (“best parameters set”) of these variables was then identified and used to carry out all the experimental tests.

2.2.1. Lock-in measurements

A schematic representation of the measuring principle is shown in Fig. 2. The IR camera was coupled to a heat source (4 × 1 kW halogen lamps) which is driven by a power amplifier and a function generator. Halogen lamps were positioned so as to produce a uniform distribution of heat across the illuminated side of the specimen. The distance of the IR camera from the sample was approximately 50 cm in order to record the entire area of the sample. The heat source and the infrared camera signals were synchronized using a lock-in amplifier (actually integrated in the camera). A photograph of a typical experimental set-up is shown in Fig. 3.

The amplitude of the periodic temperature change over the sample surface and its phase angle with respect to the applied modulated heating were calculated by processing the recorded image data using four images within one cycle; hence, for each modulation frequency, only two images are produced as output of the lock-in process. For fixed material properties, the phase delay depends onto the depth of a given defect and the excitation frequency. Therefore, the correct excitation frequency must be chosen to obtain sufficient phase contrast over the range of depths at which a defect is expected to be found. Otherwise, several tests have to be carried out changing the modulation frequency, as it was done in this study.

2.2.2. Pulsed phase measurements

A schematic representation of the measuring principle is shown in Fig. 4. Instead of making use of a sinusoidal modulation, the specimen is pulse heated using either halogen lamps (long pulse>500 ms) or high power xenon tube ring flashes (short pulse<1 ms). Consequently, thermal waves of different frequencies are launched into the specimen simultaneously and the resulting temperature field of its surface is measured in the transient regime.

Extraction of the various frequencies was performed by acquiring a sequence of infrared images and extracting the temporal decay of each pixel in the field of view. Then the discrete one-dimensional Fourier transform (DFT) was applied on each pixel

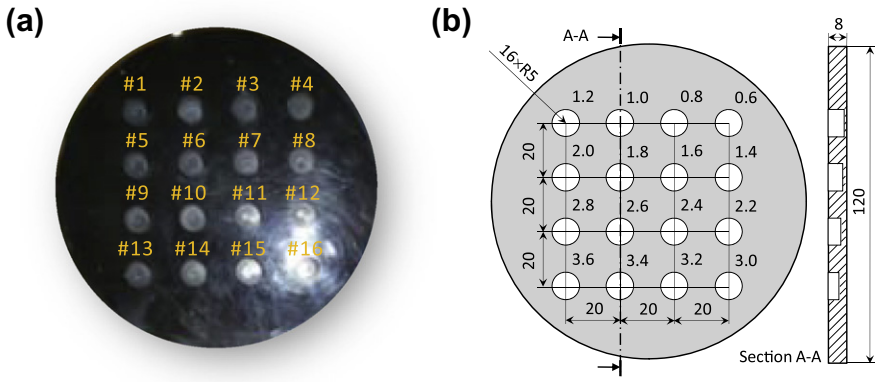

Fig. 1. PMMA reference specimen with flat-bottomed holes of different depths: (a) rear side of the specimen and (b) drawing showing nominal dimensions (in mm) and relative position of defects.

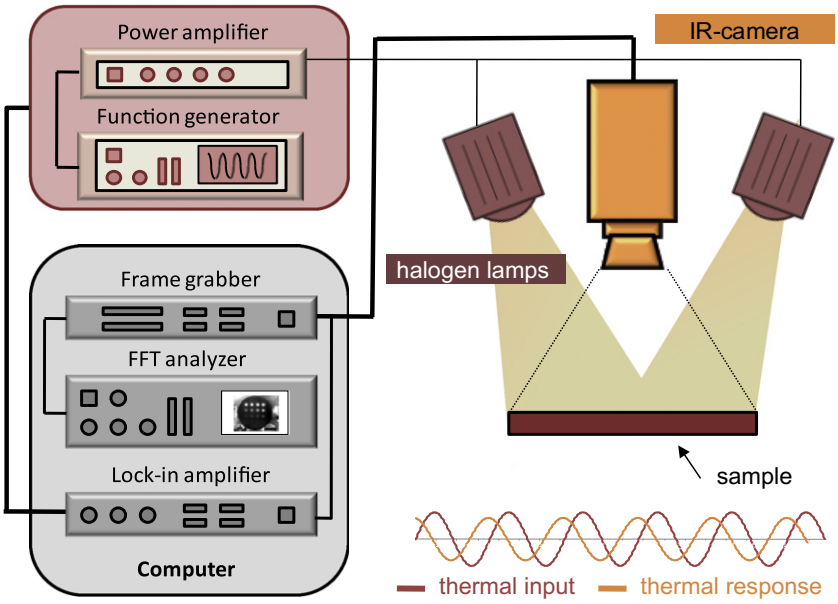

Fig. 2. Lock-in infrared thermography measuring principle.

Fig. 3. Experimental set-up for lock-in measurements.

of the thermogram sequence to compute the real and imaginary parts and, finally, amplitude and phase images were calculated. The range of frequencies span from 0 to $1/\Delta t$ (i.e., the frame rate), where Δt is the time interval between the images in the recorded sequence, while the frequency resolution is given by $\Delta f = 1/(N\Delta t)$, being N the number of thermal images in the sequence. The maximum frequency available is thus limited by the frame rate, while the frequency resolution is limited by the duration of the experiment.

2.3. Thermal diffusivity measurements

For quantitative non-destructive evaluation of subsurface defects the thermal diffusivity α of the material must be known, as will be pointed out in next section with more details. Unfortunately, the exact value of this parameter is not always available in the literature.

To overcome this problem, a fast simple transient thermographic method based on thermal pulse stimulation was used. The proposed approach exploits the well known Parker's law [22]:

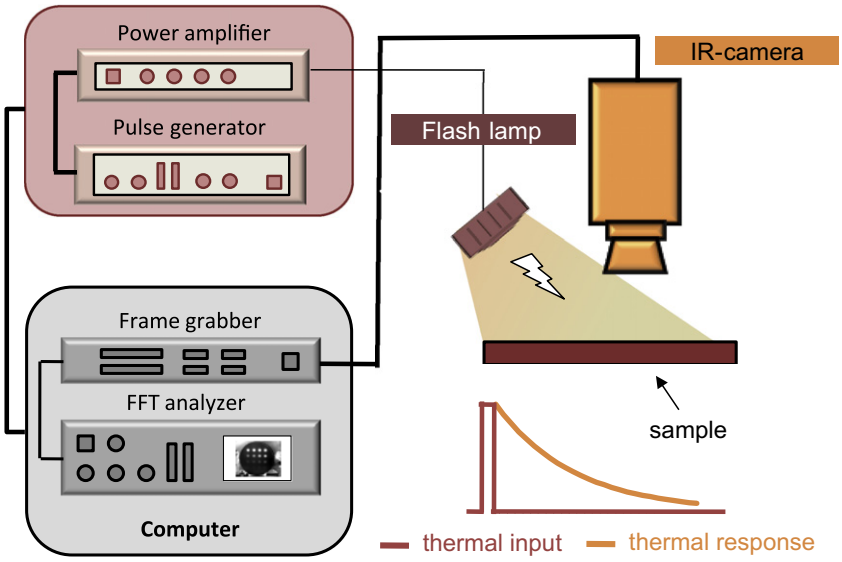

Fig. 4. Pulsed infrared thermography measuring principle.

$$\alpha = 0.1388\frac{h^2}{t_{0.5}} \tag{1}$$

where h is the sample thickness and $t_{0.5}$ the half temperature rise time, that is the time needed to reach one half of the maximum temperature increment over the sample surface opposite to the heated one. The simple ideal model of the flash method as proposed by Parker et al. is based on the analytical solution of the Fourier equation applied to a homogeneous opaque thermally insulated infinite slab uniformly subjected to a Dirac pulse of radiant energy over its surface. In its usual implementation the flash method consists of heating the front face of a small disk-shaped sample by a laser pulse and monitoring, under laboratory conditions, the temperature evolution over a very small area of its rear surface (with either a single point IR detector or a thermocouple). Here a high power flash was used to generate a sudden energy pulse (duration $\sim$ 1 ms) on the front surface of the sample while the resulting temperature response was measured in the transient phase by the IR camera in a transmission mode configuration. Fig. 5 shows the relative temperature increment measured over a small area of a defect-free PMMA sample. Measurements were performed at room temperature (23 °C) under atmospheric pressure. Only the central part of the heated zone was used for thermal diffusivity computation.

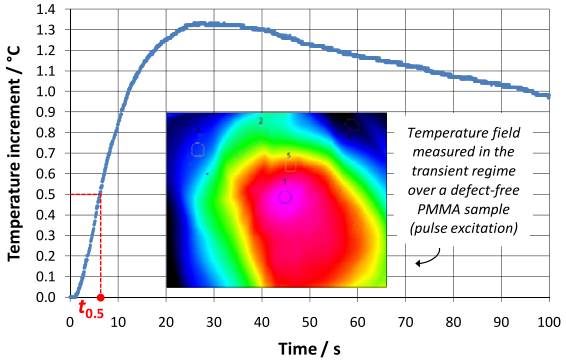

Fig. 5. Measurement of the material thermal diffusivity by means of a fast IR transient flash method: normalized temperature increments vs. heating time.

Since the measurement of the thermal transient for the computation of the thermal diffusivity is performed on a relatively large area, local values could be averaged, thus improving the signal to noise ratio. On the other hand, the simplified experimental approach may lead to an overestimation of the thermal diffusivity value, due to convection and radiation heat losses that might occur between the sample and the surrounding environment. The effect of heat losses is however limited due to the very small temperature increment actually needed because of the high thermal sensitivity of the IR camera. In addition, the accuracy of the method could be further improved by using specific non-linear interpolation models which take into account the actual heat exchange conditions [23–25].

In order to assess the accuracy of the proposed approach both type A and type B uncertainty sources have to be taken into account (Table 1); then, the combined standard uncertainty of thermal diffusivity measurement can be estimated according to GUM [26]. The ±4.9% type A component quotes the random variability observed on 15 independent repeated measurements carried out on nominally identical samples. Type B components include sources of uncertainty associated with the measurement of the sample thickness, the performance of the detection system (IR camera), the steady state temperature of the sample, the time base reference and the effects of heat losses. The sample thickness h was measured using a caliper having a rated resolution of 0.05 mm: since the thermal diffusivity α is related to the square of the

Table 1
Uncertainty analysis of thermal diffusivity measurements.

Uncertainty sources	Type[a,b]	$\frac{u(x_i)}{x_i}$	$\sqrt{\sum_{i=1}^{n}\left(\frac{u(x_i)}{x_i}\right)^2}$
Random variability	A	± 4.9%	4.9%
Sample thickness	B	± 1.3%	
IR camera	B	± 0.1%	
Absolute sample temperature	B	± 0.6%	2.1%
Time scale and time origin	B	± 0.1%	
Heat losses	B	± 1.5%	
Combined standard uncertainty $u_c(\alpha)/\alpha$			5.3%

[a] Type A uncertainty calculated as standard deviation of the mean of 15 independent measurements.
[b] Type B uncertainties calculated as $u(x_i) = \pm a/\sqrt{3}$ where a is the half-width of the assumed variability interval.

sample thickness (1) then the relative error $\Delta\alpha/\alpha$ equals to $2\Delta h/h$, resulting in a relative uncertainty of ±1.3% for a 2.2 mm sample thickness. The performance of the IR system in measuring small temperature differences is limited by the infrared camera intrinsic noise level (NETD), which is typically less than 25 mK at ambient temperature. The errors associated with the 14-bit A/D conversion are extremely small and can be neglected. Hence, as measurements had been performed at ambient temperature (23 °C), the uncertainty associated with the detection system was estimated to be ±0.1%. To assess the thermal stability, the sample rear face temperature was monitored by means of the IR camera before heat pulse application. The manufacturer specified a temperature measurement accuracy of ±1 °C or ±1% over the calibrated range (from 5 °C to 300 °C): by assuming a uniform distribution throughout that interval, a ±0.6% relative uncertainty contribution was estimated. Given that the measurement of α relies on the temperature rise vs. time evolution, the accuracy of the time origin is of primary importance. The flash generation unit has a response time smaller than 500 ns while thermal images are acquired at 80 Hz (i.e., 12.5 ms sampling rate): as the half temperature rise time for a PMMA sample 2.2 mm thick is about 6.2 s, the relative amplitude of the error associated with the time origin (i.e., origin of the energy pulse) measurement can be estimated to be ±0.0125/6.2 or ±0.2%. Finally, as heat losses by convection and radiation between the sample and the environment are concerned (a ceramic sample holder was used to limit conductive heat flows between the sample and its support), it was assumed that they account for a further ±2.6% variability on the thermal diffusivity measurement. This conclusion is based on the ±1.3% estimation already reported in literature for the laser flash method applied to steel samples placed into a vacuum chamber [27], which was doubled considering the less controlled environmental conditions of the current experimental set-up as well as the low thermal diffusivity of PMMA ($\alpha = 0.108$ mm^2/s).

By taking into account the different sources of errors the uncertainty budget is build up as shown in Table 1.

3. Results and discussion

3.1. Amplitude and phase angle thermal images

Lock-in (LT) amplitude and phase images of the reconstructed thermal wave on the reference specimen surface are reported in Fig. 6 for different modulation frequencies.

As it can be observed, the information given by the phase image is actually more effective, since it is relatively independent of local optical (e.g., non-uniform heating) and infrared (e.g., variability in surface emissivity) surface features. As a consequence, only signal amplitude is affected by the specimen topography while phase is not, except for the level of phase noise which of course increases in parts where less light is absorbed per unit area.

At 2.250 Hz, the relatively high modulation frequency limits the analysis to a close to the surface region, where black coating disuniformity can be appreciated in the phase image. By reducing the lock-in frequency, deeper defects are progressively revealed.

In the mid-high range (0.100 Hz < f < 0.025 Hz) the first two rows are clearly visible: in the phase images, defects appear brighter than the surrounding background (i.e., they exhibit a positive phase difference with respect to the background defect free material) and their boundaries are well defined.

The third row starts to come out for modulation frequencies in the mid-low range (0.015 Hz < f < 0.008 Hz). At this stage, the sharpness of the shallower defects in the first row becomes poor.

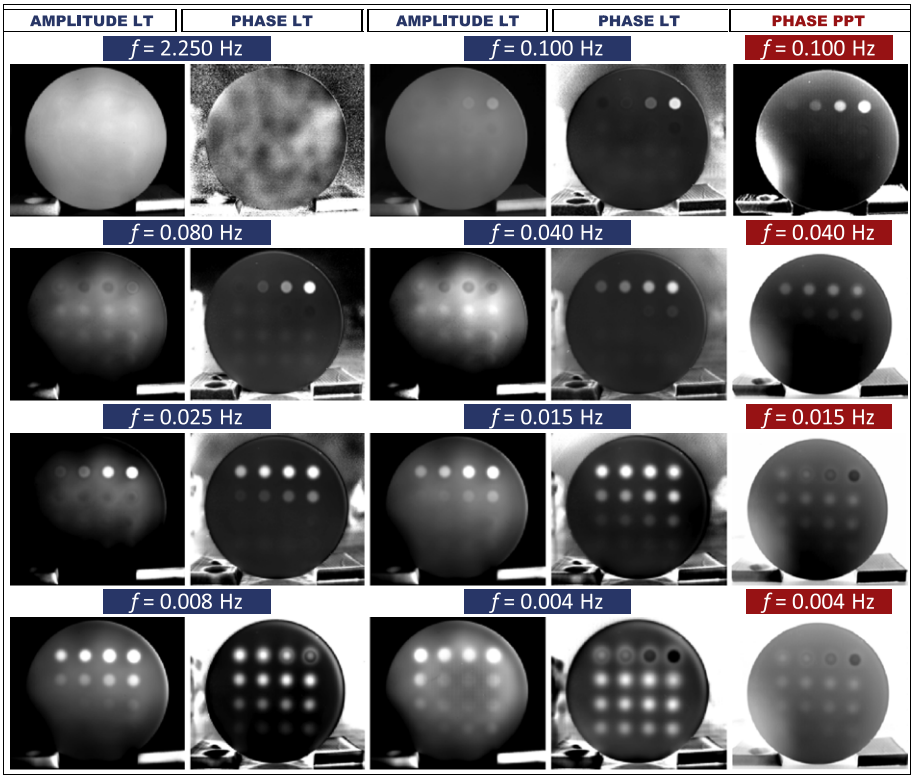

Fig. 6. Lock-in IR measurements (LT): amplitude (left) and phase (right) images of the reconstructed thermal wave on the reference specimen surface obtained at different modulation frequencies. Pulse phase IR measurements (PPT): phase images obtained by unscrambling the frequency content of the infrared images sequence measured after thermal pulse stimulation using the discrete Fourier transform.

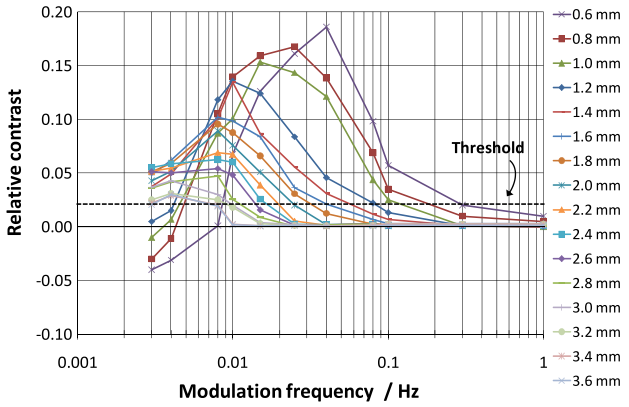

Fig. 7. Relative contrast curves computed over each region of interest as a function of the modulation frequency. Each curve in the figure is labelled with a number showing the actual defect depth. The threshold value corresponds to a relative contrast equal to 0.022.

At 4 mHz, also the deepest flat-bottomed hole is detected, although the contrast with the background is remarkably lowered due to a noteworthy reduction in the phase shift. Moreover, at very low frequency the boundary of the defects in the thermal image seems to be "out of focus", because of significant radial heat diffusion that takes place in the specimen plane. In addition, the shallower defects in the first row exhibit a phase inversion (see also Fig. 7) due to a matched combination of depth–diameter-modulation frequency, resulting in little or no phase response (blind frequency [28]). Pickering and Almond [14] and Wallbrink et al. [30] already observed the same effect for flat-bottomed artificial defects back-drilled in carbon fibre composite and steel plates, respectively, and concluded that blind frequency occurrence is related to the defect diameter/thermal diffusion length ratio. In our study we found that it also depends on the depth of the defect and appears for p/μ^* ratios higher than 0.30.

The observed frequency-dependent behaviour is a direct consequence of the inverse relationship existing between the thermal diffusion length μ and the modulation frequency f [29]:

$$\mu = \sqrt{\frac{2k}{\rho\omega c}} = \sqrt{\frac{\alpha}{\pi f}} \tag{2}$$

being $\omega = 2\pi f$ the angular frequency of the modulation, k the thermal conductivity of the material, ρ the density, c the specific heat and α the thermal diffusivity.

Similar results (Fig. 6, last column) were obtained by unscrambling the frequency content of the infrared images sequence measured after thermal pulse stimulation (PPT, pulse phase approach). With respect to the lock-in technique, this method has the advantage of being faster, since it might necessitate just one measurement to analyze the whole frequency range of interest, whereas the lock-in approach requires multiple iterative tests. Phase contrast however is poorer, hiding the detection of deeper flaws. Indeed, pulse-phase results display more defects at the highest frequencies and fewer at the lower frequencies. To explain the observed behaviour it should be considered that the thermal pulse used to heat the sample has a finite temporal duration. Hence, the available energy and amplitudes are not uniformly distributed along the whole frequency spectrum. The theoretical analysis of the spectrum shape shows that longer pulses in the time domain (in this case a 2 s heat pulse was used) tends to concentrate the energy in the lower frequencies. This in turn activates complex heat diffusion mechanisms that are no longer one-dimensional. As a consequence phase reversal occurs at frequencies that are higher with respect to the lock-in case. One further drawback of the pulse phase approach is that a definite temperature difference between two successive images of the sequence must exist to clearly discern defects. To display discontinuities located more in depth a higher surface heating is needed.

3.2. Estimation of defects depth

By assuming a one-dimensional pure conduction heat transfer model, the resulting temperature T as a function of depth z and time t, for a homogeneous semi-infinite planar specimen subjected to uniform periodical heat deposition (at $z = 0$) with modulation frequency ω is given by [29]:

$$T(z,t) = T_0 \exp\left(-\frac{z}{\mu}\right) \exp i\left(\omega t - \frac{z}{\mu}\right) = A(z) \exp i(\omega t - \varphi(z)) \tag{3}$$

where $A(z)$ is the thermal amplitude and $\varphi(z)$ the phase shift of the thermal wave travelling inside the material. This equation underlines the direct relationship existing, under the assumed hypothesis, between the phase angle of the thermal wave and the defect depth/thermal diffusion length ratio. For the phase image, the maximum depth range that can be inspected roughly corresponds to 1.8μ [4,29]. Hence, as shown in (2), the actual depth of the defect depends, for a given material, upon the modulation frequency at which the defect itself is first detected.

To determine unambiguously this frequency, the relative contrast was first defined as follows:

$$C(f) = \frac{S_{def}(f) - S_b(f)}{S_b(f)} \tag{4}$$

where S_{def} and S_b are phase angle values measured, at modulation frequency f, over defected and sound areas, respectively. The absolute phase contrast was evaluated using a spatial reference technique obtained by subtracting the average phase angle in the sound material (S_b) from the phase angle measured over the defects (S_{def}) on a centrally located circular area. This value was then normalized by dividing it by the average phase angle in the sound material (S_b) to get the relative contrast.

Then, for each region of interest, C values were plotted as a function of the modulation frequency (Fig. 7).

To determine the frequency at which each defect had been first detected (f_{TR}), a threshold level C_{TR} was defined, so that for $C \geqslant C_{TR}$ the discontinuity was assumed detectable, while for $C < C_{TR}$ it was not. The threshold value was determined by taking into account the background noise,[1] which was estimated, for each excitation frequency, by means of the standard deviation σ_b of phase angles values measured over the sound region of the material. If we assume that phase angle measurements over the defects contain the same level of noise (i.e., $\sigma_{def} = \sigma_b$) then the threshold value below which detection of defects becomes hidden by the noise can be calculated as:

$$C_{TR} = \frac{2\sigma_b + 2\sigma_{def}}{S_b} \tag{5}$$

in which two standard deviations were used to represent 95% confidence levels. Since C_{TR} changes slightly with the excitation frequency, the average value ($C_{TR} = 0.022$) was considered.

The frequency of first appearance was determined, for each defect, by performing a linear interpolation between the coordinates (f_x, C_x) of the two closest experimental points and by calculating the exact frequency f_{TR} at which the interpolation line crosses the threshold value.

[1] The noise in the thermal image results from several sources such as detector noise (which is accounted for by the NETD), inspected material (thermal conductivity, thermal diffusivity), and heating parameters (light intensity and distribution, orientation of the lamps relative to the camera).

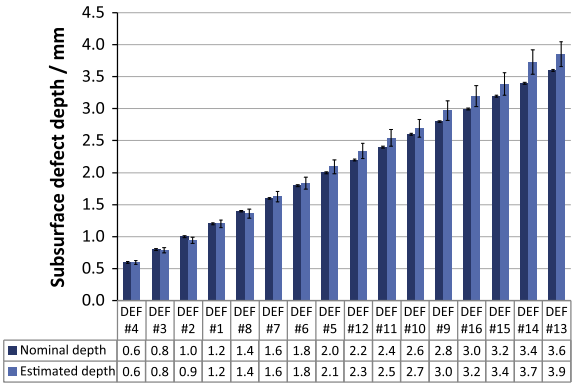

Fig. 8. Quantitative non-destructive evaluation of subsurface defects: comparison of estimated and nominal defects depth.

Table 2
Comparison between estimated and nominal defects depths.

Label	p_{nom} (mm)	$u(p_{nom})$ (mm)	p_{meas} (mm)	$u(p_{meas})$ (mm)	Error (%)
DEF #4	0.600	±0.014	0.60	±0.03	−0.1
DEF #3	0.800	±0.014	0.79	±0.04	−1.7
DEF #2	1.000	±0.014	0.94	±0.05	−5.6
DEF #1	1.200	±0.014	1.20	±0.06	0.2
DEF #8	1.400	±0.014	1.36	±0.07	−2.7
DEF #7	1.600	±0.014	1.63	±0.08	1.8
DEF #6	1.800	±0.014	1.84	±0.09	2.1
DEF #5	2.000	±0.014	2.09	±0.11	4.7
DEF #12	2.200	±0.014	2.34	±0.12	6.5
DEF #11	2.400	±0.014	2.54	±0.13	6.0
DEF #10	2.600	±0.014	2.70	±0.14	3.8
DEF #9	2.800	±0.014	2.97	±0.15	6.2
DEF #16	3.000	±0.014	3.20	±0.16	6.6
DEF #15	3.200	±0.014	3.39	±0.17	5.9
DEF #14	3.400	±0.014	3.73	±0.19	9.7
DEF #13	3.600	±0.014	3.85	±0.20	7.0

Finally, the depth of each defect was assessed using the equation:

$$p = 1.8\mu = 1.8\sqrt{\frac{\alpha}{\pi f_{TR}}} \tag{6}$$

Fig. 8 and Table 2 report the comparison between estimated and nominal defects depth.

Uncertainty bands for nominal depth values (Fig. 8 and Table 2) were calculated as type B by assuming a rectangular distribution of width R, where $R = 0.05$ mm is the resolution of the caliper used to measure the depth of the reference specimen flat-bottomed holes. Uncertainty bands for estimated defect depth values (Fig. 8, Tables 2 and 3) were instead computed as combined standard uncertainty considering the contributions of f_{TR} and α:

$$u^2(p) = \sum_{x_i=\alpha,\ f_{TR}} \left(\frac{\partial p}{\partial x_i}\right)^2 u^2(x_i) \tag{7}$$

which yields

$$\left[\frac{u(p)}{p}\right]^2 = \frac{1}{4}\left[\frac{u(\alpha)}{\alpha}\right]^2 + \frac{1}{4}\left[\frac{u(f_{TR})}{f_{TR}}\right]^2 \tag{8}$$

Relative percentage errors of depths estimation (Table 2) range from −0.1% (defect #4, 0.60 mm deep) to +9.7% (defect #14, 3.4 mm deep). These results are consistent with the estimated measurement uncertainty at 95% confidence level ($U(p)/p = ku(p)/p = \pm 10.7\%$, coverage factor $k = 2.1$ based on a t distribution with 16 degree of freedom). It can be noted that the estimation error increases with the depth of the defect (i.e., at very low excitation frequency). Since the adopted photothermal model assumes 1D heat propagation, this means that the actual heat flow within the specimen is moving into the 3D domain. The transition from predominantly one-dimensional heat flow to two-dimensional heat flow is further confirmed by the phase angle reversal observed over the shallower defects for frequencies below 0.006 Hz (Fig. 7). Actually, retrieving the depth of deeper defects with greater accuracy requires solving the two-dimensional heat propagation in order to account for border effects.

Table 3
Uncertainty analysis of defects depth estimation.

Label	p_{nom} (mm)	f_{TR} (Hz)	$u(f_{TR})/f_{TR}$ [a]	α (mm²/s)	$u(\alpha)/\alpha$ [b]	p_{meas} (mm)	$u(p_{meas})/p_{meas}$
DEF #4	0.600	0.310	0.087	0.108	0.053	0.60	0.05
DEF #3	0.800	0.180	0.087	0.108	0.053	0.79	0.05
DEF #2	1.000	0.125	0.087	0.108	0.053	0.95	0.05
DEF #1	1.200	0.077	0.087	0.108	0.053	1.20	0.05
DEF #8	1.400	0.060	0.087	0.108	0.053	1.36	0.05
DEF #7	1.600	0.042	0.087	0.108	0.053	1.63	0.05
DEF #6	1.800	0.033	0.087	0.108	0.053	1.84	0.05
DEF #5	2.000	0.025	0.087	0.108	0.053	2.10	0.05
DEF #12	2.200	0.020	0.087	0.108	0.053	2.35	0.05
DEF #11	2.400	0.017	0.087	0.108	0.053	2.55	0.05
DEF #10	2.600	0.015	0.087	0.108	0.053	2.70	0.05
DEF #9	2.800	0.013	0.087	0.108	0.053	2.98	0.05
DEF #16	3.000	0.011	0.087	0.108	0.053	3.20	0.05
DEF #15	3.200	0.010	0.087	0.108	0.053	3.39	0.05
DEF #14	3.400	0.008	0.087	0.108	0.053	3.74	0.05
DEF #13	3.600	0.008	0.087	0.108	0.053	3.86	0.05

[a] Type B uncertainty calculated as $u(f_{TR}) = \pm a/\sqrt{3}$, where $a = 0.15 \times f_{TR}$ (15% of the actual first detection frequency value) is the assumed variability interval half-width.
[b] Combined standard uncertainty (see Table 1).

3.3. Estimation of defects size

As far as defects size assessment is concerned, obviously the best accuracy can be achieved when the phase contrast between defected and sound areas is maximized.

Hence, starting from the relative contrast vs. modulation frequency plots, the frequency f_{max} (for which it results $C = C_{max}$) was first estimated for each region of interest (Fig. 9).

Then, the nearer available (i.e., such that $f \cong f_{x\_max}$) lock-in phase image was selected. The image file was hence post-processed through different steps (filtering, image calibration,

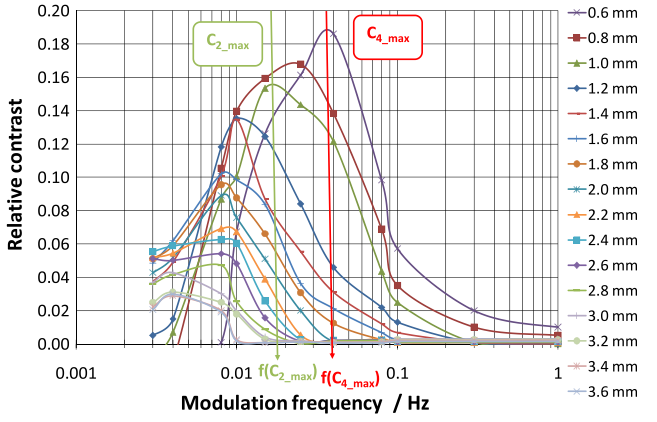

Fig. 9. Assessment of the maximum relative contrast modulation frequency for each region of interest. Each curve in the figure is labelled with a number showing the actual defect depth.

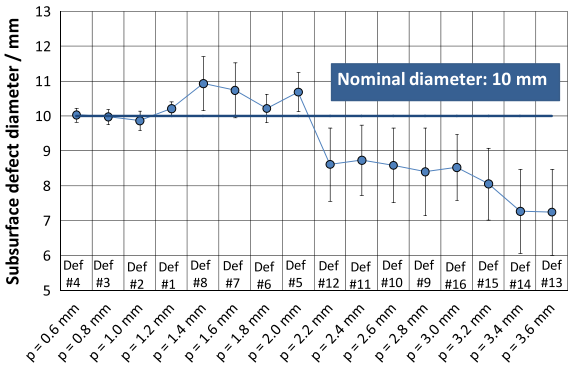

Fig. 10. Quantitative non-destructive evaluation of subsurface defects: comparison of estimated and nominal defects size.

Table 4
Comparison between estimated and nominal defects sizes.

Label	p_{nom} (mm)	d_{nom} (mm)	$u(d_{nom})$ (mm)	d_{meas} (mm)	$u(d_{meas})$ (mm)	$u(d_{meas})/d_{meas}$	Error (%)
DEF #4	0.600	10.000	±0.014	10.04	±0.20	2.0E−02	0.4
DEF #3	0.800	10.000	±0.014	9.98	±0.22	2.2E−02	−0.2
DEF #2	1.000	10.000	±0.014	9.88	±0.28	2.8E−02	−1.2
DEF #1	1.200	10.000	±0.014	10.22	±0.20	2.0E−02	2.2
DEF #8	1.400	10.000	±0.014	10.93	±0.78	7.1E−02	9.3
DEF #7	1.600	10.000	±0.014	10.74	±0.78	7.3E−02	7.4
DEF #6	1.800	10.000	±0.014	10.22	±0.40	3.9E−02	2.2
DEF #5	2.000	10.000	±0.014	10.69	±0.56	5.3E−02	6.9
DEF #12	2.200	10.000	±0.014	8.62	±1.05	1.2E−01	−13.8
DEF #11	2.400	10.000	±0.014	8.74	±1.01	1.2E−01	−12.6
DEF #10	2.600	10.000	±0.014	8.59	±1.07	1.2E−01	−14.1
DEF #9	2.800	10.000	±0.014	8.41	±1.26	1.5E−01	−15.9
DEF #16	3.000	10.000	±0.014	8.53	±0.94	1.1E−01	−14.7
DEF #15	3.200	10.000	±0.014	8.06	±1.03	1.3E−01	−19.4
DEF #14	3.400	10.000	±0.014	7.28	±1.20	1.6E−01	−27.2
DEF #13	3.600	10.000	±0.014	7.25	±1.23	1.7E−01	−27.5

overlaying of predefined geometrical objects, and measurement of the defect area) by means of dedicated digital image processing software written in Labview™. Otherwise, defects size could also be determined with comparable accuracy by means of the shearing-phase profile obtained by pixel subtraction [13].

Results are reported in Fig. 10, where they are compared with the nominal diameter value.

Uncertainty bands (Fig. 10 and Table 4) were calculated as standard deviations on three measurements carried out with slightly different geometrical circles in order to take into account data variability induced by unsharpened defect boundaries.

Relative percentage errors (Table 4) of size estimation range from about 2% for the shallower defects in the first row to 28% for the deepest one (defect #13, 3.6 mm deep). The relative high errors found, in particular for the deeper defects (located in the lower two rows), can be attributed to the limited number of experimental data (i.e., modulation frequency steps) and to significant radial heat diffusion, that made measurement of the actual hole boundary quite difficult.

Similar results were found by post-processing the thermograms obtained using the pulse phase approach, although, with the current working parameters (one flash with pulse duration 2 s, heating energy 7.2 kJ) it was not possible to detect defects located more than 3 mm beneath the front surface of the reference specimen. The detailed analysis is not reported here however.

4. Conclusions

Active thermography measurement techniques have been exploited for quantitative assessment of subsurface defects in a reference specimen made of Plexiglas. By proper post-processing of phase thermal images recorded at different frequencies and direct measurement of material's thermal diffusivity, a fast, contactless and effective NDE methodology has been demonstrated.

Lock-in thermography provides quantitative information about size, depth and thermal resistance of defects and, as phase images are used, relatively insensitivity to non-uniform heating and local variation of the emissivity coefficient. The main limitation of this technique relies on the very low heat flux modulation frequency required to detect deeper defects in Plexiglas. In addition, multiple tests are usually needed to evaluate the whole range of depths at which a defect is expected to be found. Hence, the measurement process can turn out to be quite time-consuming.

Pulse phase thermography is in principle faster than lock-in. However, there are also some limitations: the main one is that to display deeper defects a higher surface heating is usually required (which may damage plastic materials), because significantly less energy is being applied at each of the frequencies that are extracted using the FFT, as opposed to all of it at the frequency of interest in the case of lock-in.

The results reported in this work were obtained by using a reference panel containing artificial flat-bottomed holes defects. Real defects, such as delaminations and cracks in fibre reinforced composites or voids, shrinkage and inclusions in castings, are different from artificial ones. Variables like defect thickness and orientation are thought to be important in determining the actual thermal path within the material and might strongly affect the sizing accuracy as well as depth estimation.

Acknowledgments

The author would like to thank S. Aliquò for her assistance in performing the experimental tests. A special thank is reserved to Prof. G. Busse and his research group at the IKP-ZfP Institute of the University of Stuttgart (D) for their kindly support and precious advices.

References

[1] Annual Infrared Thermography Applications Conference (ThermoSense), Proceedings of SPIE, Bellingham, WA. <http://thermosense.org/>.
[2] Biannual Quantitative Infrared Thermography Conference (QIRT), Université Laval, Quebec City, Canada. <http://qirt.gel.ulaval.ca/>.
[3] D. Wu, G. Busse, Lock-in thermography for nondestructive evaluation of materials, Rev. Gén. Therm. 37 (1998) 693–703.
[4] C. Meola, G.M. Carlomagno, Recent advances in the use of infrared thermography, Meas. Sci. Technol. 15 (2004) R27–R58.
[5] C. Meola, G.M. Carlomagno, A. Squillace, G. Giorleo, Non-destructive control of industrial materials by means of lock-in thermography, Meas. Sci. Technol. 13 (2002) 1583–1590.
[6] C. Meola, G.M. Carlomagno, G. Giorleo, The use of infrared thermography for materials characterization, J. Mater. Process. Technol. 155–156 (2004) 1132–1137.
[7] N.P. Avdelidis, D.P. Almond, A. Dobbinson, B.C. Hawtin, C. Ibarra-Castanedo, X. Maldague, Aircraft composites assessment by means of transient thermal NDT, Prog. Aerosp. Sci. 40 (2004) 143–162.
[8] T. Inagaki, T. Ishii, T. Iwamoto, On the NDT and E for the diagnosis of defects using infrared thermography, NDT&E Int. 32 (1999) 247–257.
[9] G.M. Carlomagno, P.G. Berardi, Unsteady thermo-topography in non-destructive testing, in: Infrared Information Exchange, vol. III, St. Louis, Missouri, 1976, pp. 33–40.
[10] G. Busse, A. Rosencwaig, Subsurface imaging with photoacoustics, Appl. Phys. Lett. 36 (1980) 815–816.
[11] G. Busse, D. Wu, W. Karpen, Thermal wave imaging with phase sensitive modulated thermography, J. Appl. Phys. 71 (1992) 3962–3965.
[12] T. Sakagami, S. Kubo, Applications of pulse heating thermography and lock-in thermography to quantitative nondestructive evaluations, Infrared Phys. Technol. 43 (2002) 211–218.
[13] M. Choi, K. Kang, J. Park, W. Kim, K. Kim, Quantitative determination of a subsurface defect of reference specimen by lock-in infrared thermography, NDT&E Int. 41 (2008) 119–124.
[14] S. Pickering, D. Almond, Matched excitation energy comparison of the pulse and lock-in thermography NDE techniques, NDT&E Int. 41 (2008) 501–509.

[15] D. Wu, Lockin thermography for defect characterization in veneered wood, in: QIRT 94 Sorrento, Italy, 1994, pp. 298–302.
[16] W. Karpen, D. Wu, R. Steegmuller, G. Busse, Depth profiling of orientation in laminates with local lock-in thermography, in: QIRT 94 Sorrento, Italy, 1994, pp. 281–286.
[17] E. Grinzato, P. Bison, S. Marinetti, V. Vavilov, Nondestructive evaluation of delaminations in fresco plaster using transient infrared thermography, Res. Nondestruct. Eval. 5 (1994) 257–274.
[18] G.M. Carlomagno, C. Meola, Comparison between thermographic techniques for frescoes NDT, NDT&E Int. 35 (2002) 559–565.
[19] E. Grinzato, P. Bison, C. Bressan, A. Mazzoldi, NDE of frescoes by infrared thermography and lateral heating, in: QIRT 98 Lodz, Poland, 1998, pp. 64–70.
[20] X. Maldague, S. Marinetti, Pulse phase infrared thermography, J. Appl. Phys. 79 (1996) 2694–2698.
[21] X. Maldague, F. Galmiche, A. Ziadi, Advances in pulsed phase thermography, Infrared Phys. Technol. 43 (2002) 175–181.
[22] W.J. Parker, R.J. Jenkins, C.P. Butler, G.L. Abbot, Flash method of determining thermal diffusivity, J. Appl. Phys. 32 (1961) 1679–1684.
[23] E. Grinzato, S. Marinetti, Materials NDE by nonlinear filtering applying heat transfer models, NATO ASI Series E: Applied Sciences, vol. 262, Kluwer Academic Publishers, 1994, pp. 117–132.
[24] P.G. Bison, S. Marinetti, A. Mazzoldi, E. Grinzato, C. Bressan, Cross-comparison of thermal diffusivity measurements by thermal methods, Infrared Phys. Technol. 43 (2002) 127–132.
[25] F. Cernuschi, P.G. Bison, A. Figari, S. Marinetti, E. Grinzato, Thermal diffusivity measurements by photothermal and thermographic techniques, Int. J. Thermophys. 25 (2004) 439–457.
[26] Guide to the Expression of Uncertainty in Measurement, UNI CEI ENV 13005, 2000.
[27] L. Vozár, W. Hohenauer, Uncertainty of the thermal diffusivity measurement using the laser flash method, in: Proceedings of Fifteenth Symposium on Thermophysical Properties, Boulder (CO), USA, 2003.
[28] W. Bai, B.S. Wong, Evaluation of defects in composite plates under convective environments using lock-in thermography, Meas. Sci. Technol. 12 (2001) 142–150.
[29] X. Maldague, Theory and Practice of Infrared Technology for Nondestructive Testing, John Wiley and Sons Inc., New York, 2001. pp. 344/358.
[30] C. Wallbrink, S.A. Wade, R. Jones, The effect of size on the quantitative estimation of defect depth in steel structures using lock-in thermography, J. Appl. Phys. 101 (2007) 1–8.